Editors' Suggestion

Phonon dispersion of the organic semiconductor rubrene

Kenta Takada,[1] Kohei Yoshimi,[2] Satoshi Tsutsui,[3,4] Koji Kimura,[5] Kouichi Hayashi,[5] Ikutaro Hamada,[6] Susumu Yanagisawa,[7] Naotaka Kasuya,[8] Shun Watanabe,[8] Jun Takeya,[8] and Yusuke Wakabayashi[1,9,*]

[1]*Department of Physics, Graduate School of Science, Tohoku University, Sendai 980-8578, Japan*
[2]*Division of Materials Physics, Graduate School of Engineering Science, Osaka University, Toyonaka 560-8531, Japan*
[3]*Japan Synchrotron Radiation Research Institute (JASRI), SPring-8, Sayo, Hyogo 679-5198, Japan*
[4]*Institute of Quantum Beam Science, Graduate School of Science and Engineering, Ibaraki University, Hitachi, Ibaraki 316-8511, Japan*
[5]*Department of Physical Science and Engineering, Nagoya Institute of Technology, Gokiso-cho, Showa-ku, Nagoya 466-8555, Japan*
[6]*Department of Precision Engineering, Graduate School of Engineering, Osaka University, 2-1 Yamada-Oka, Suita, Osaka 565-0871, Japan*
[7]*Department of Physics and Earth Sciences, Faculty of Science, University of the Ryukyus, Okinawa 903-0213, Japan*
[8]*Department of Advanced Material Science, Graduate School of Frontier Science, The University of Tokyo, 5-1-5 Kashiwanoha, Kashiwa, Chiba 277-8561, Japan*
[9]*Materials Research Center for Element Strategy, Tokyo Institute of Technology, Yokohama 226-8501, Japan*

(Received 8 March 2022; accepted 10 May 2022; published 25 May 2022)

The phonon dispersion of the organic semiconductor, rubrene, is experimentally measured by the inelastic x-ray scattering experiments performed at room temperature. In organic crystals, weak van der Waals interaction among the molecules increases the amplitude of the lattice vibration. Therefore, phonons are essential in organic crystals. However, there are few experimental reports on phonon dispersion in organic semiconductors and no reports on modern high-mobility organic semiconductors, which hampers the complete understanding of many phenomena in organic semiconductors. The dispersion of low-energy optical and acoustic phonon modes, including both intermolecular and intramolecular modes, is measured along the orthorhombic principal axes. Short-wavelength modes are expected to be affected by the anisotropic molecular shape, and the experimental result suggests that even the phonons having a wavelength of 140 Å are well modified, showing strong mixing of local and nonlocal phonon modes. This study provides a robust foundation for investigating organic semiconductors and understanding the lattice dynamics of highly anisotropic motifs.

DOI: 10.1103/PhysRevB.105.205205

I. INTRODUCTION

Lattice vibration is one of the fundamental phenomena in condensed-matter physics. It is the primary source of heat capacity and electrical resistivity. The coupling of phonons and electrons modulates electronic states, leading to interesting electronic properties, such as superconductivity or charge-density waves. In the literature, phonons are introduced with the atomistic model. However, not all materials are well approximated using isotropic atoms. Molecular or organic crystals are typical examples of such materials composed of anisotropic units. The illustration of the lattice dynamics in such materials is essential for understanding organic materials; however, this is a challenging task in solid-state physics. The anisotropic shape of molecules should affect the short-wavelength phonon eigenmodes, which can be examined only by the inelastic scattering experiments with quantum beams having a wavelength of Å.

Due to weak intermolecular interactions, the phonons in organic materials have large amplitudes, resulting in strong phonon effects on their various properties [1–5]. Organic conductors often exhibit Peierls instability [6], charge-density wave [1,7] and superconductivity [8]. The properties of organic semiconductors, which enable their application in light-emitting diodes, lasers [9], solar cells, and field-effect transistors [10–12], are also believed to be related to phonons [3,13–17]. Large Seebeck coefficients have been reported for many organic semiconductors [18–20]. This increases the research interest in low-energy optical phonon modes, as they can increase the thermal resistivity by scattering acoustic phonons.

The charge transport mechanism in organic semiconductors involves carrier scattering by nonlocal (Peierls) and local (Holstein) carrier–phonon coupling [2,3,21]. The local phonon modes modulate the energy of the molecular orbital, which scatters the carrier, leading us to the classical Marcus theory of electron transfer [2]. The other extreme, nonlocal phonon side, is the rigid molecule model. It works rather well for the vibrational property of simple rigid molecules, such as acenes [22,23]. For the charge transport in acenes, nonlocal phonon dispersion is reported to have significant importance [24–26]. The mixing effect of the intramolecular modes compared to that of the intermolecular modes is more significant in the typical high-mobility organic semiconductor, rubrene [26–30], which has phenyl groups extended from the tetracene backbone. Therefore, the lattice dynamics for both inter- and intramolecular vibration are essential.

*wakabayashi@tohoku.ac.jp

Unfortunately, experimental studies on the phonon dispersion of organic semiconductors are scarce. Only the deuterated naphthalene crystal has been measured using the inelastic neutron-scattering experiment [22]. The neutron-scattering experiment requires deuteration to reduce the strong background intensity caused by the incoherent scattering of protons. However, this substitution alters the lattice vibration frequency [31], as well as the electronic property of molecular crystals [32,33]. In this study, we measured the phonon dispersion of rubrene, one of the most studied organic semiconductors [3,4,11,12,18,20,34,35], by the inelastic x-ray scattering (IXS) technique. This technique allows us to measure the phonons of molecules with many protons without deuteration. In addition, a well-focused synchrotron beam enables the measurement of the phonon excitation from one piece of a small single crystal.

II. EXPERIMENTS

Throughout this paper, we employ the orthorhombic unit cell with the space group *Bbam* [36]. Thin plate-shaped single crystal samples were grown by the physical vapor transport method. The typical size of the crystals used was 4 mm × 1 mm × 0.1 mm along the a, b, and c directions. X-ray thermal diffuse scattering (TDS) measurements were performed with a four-circle diffractometer attached to an 18 kW Mo $K\alpha$ x-ray generator. The incident x-ray beam was monochromatized with a bent graphite monochromator, and the scattered beam was measured using a CdTe detector. The Bragg peak positions were not measured to prevent the detector from saturation. The air-scattering background was measured by successive measurements without the sample. The IXS measurement was performed at BL35XU of SPring-8, Japan with a 21.747 keV x ray provided by the Si 11 11 11 backscattering monochromator optics [37]. The energy resolution of the optics was 1.5 meV. The typical detector acceptance in the reciprocal space is smaller than 0.12 reciprocal lattice unit (r.l.u.) in the a^* direction and 0.24 r.l.u. in the b^* and c^* directions. The detector center measures on the intended lines within this acceptance range. All the measurements were performed at room temperature in air. To avoid radiation damage, the sample was replaced every 24 h of the synchrotron experiment.

Density functional theory (DFT) calculations were performed using the projector augmented wave (PAW) [38] method as implemented in the QUANTUM ESPRESSO [39,40] package. The wave functions and charge densities were expanded in terms of the plane-wave basis set with the kinetic energy cutoffs of 100 and 1000 Ry, respectively. We employed the rev-vdW-DF2 [41] functional for the exchange-correlation energy and potential. The PAW potentials were constructed using input files adopted from the PSlibrary [42] (version 1.0) and the exchange-correlation functional, which is consistent with the rev-vdW-DF2 functional [43]. Calculations were performed on a primitive cell containing two rubrene molecules, and the Brillouin zone integration was performed using a 2 × 2 × 2 **k**-point mesh. Atomic positions, as well as the cell degrees of freedom, were relaxed until the maximum force decreased to a value smaller than 10^{-4} Rydberg/bohr. The harmonic phonon frequencies were obtained by linear response formalism [44]. The elastic constants were derived from stress tensor calculated as a function of the strain up to ±1.5% of the lattice parameters using the THERMO_PW [45].

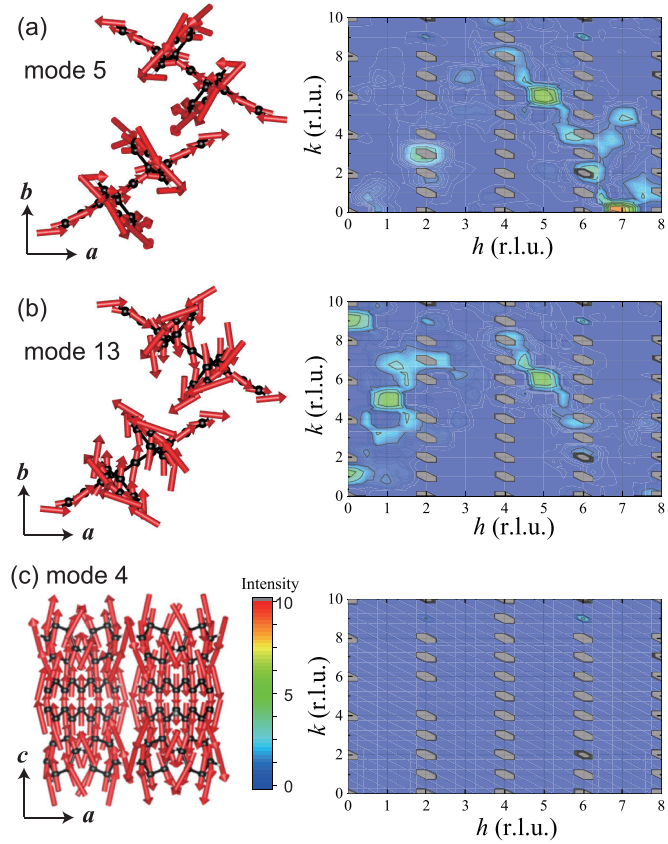

FIG. 1. Left: Calculated eigenmodes at the Γ point. Right: The intensity distribution of the TDS on the (hk0) plane calculated with the Einstein approximation for (a) mode 5-, (b) mode 13-, and (c) mode 4-character phonon branches.

III. RESULTS AND ANALYSIS

A. DFT calculations

The experimentally reported lattice parameters a, b, and c at 20 K are 7.1599, 14.1519, and 26.795 Å, respectively [35]. The optimized cell parameters based on our DFT calculations are $a = 7.159$ Å, $b = 14.093$ Å, and $c = 26.663$ Å. The difference between them is less than 0.5%. The eigenenergies and eigenmodes of the lattice vibration along the high symmetry directions in the Brillouin zone were obtained by the DFT calculation. The modes are numbered in the order of increasing energy at the Γ point. The first three modes are acoustic modes, while the rest are optical modes. Some examples of the eigenmodes are shown in Fig. 1. Details are provided in the Supplemental Material [46].

B. Thermal diffuse scattering

The thermal diffuse scattering (TDS) intensity distribution on the (hk0), (h0l), and (0kl) planes are shown in Figs. 2(a)–2(c). The air-scattering and linear background were subtracted

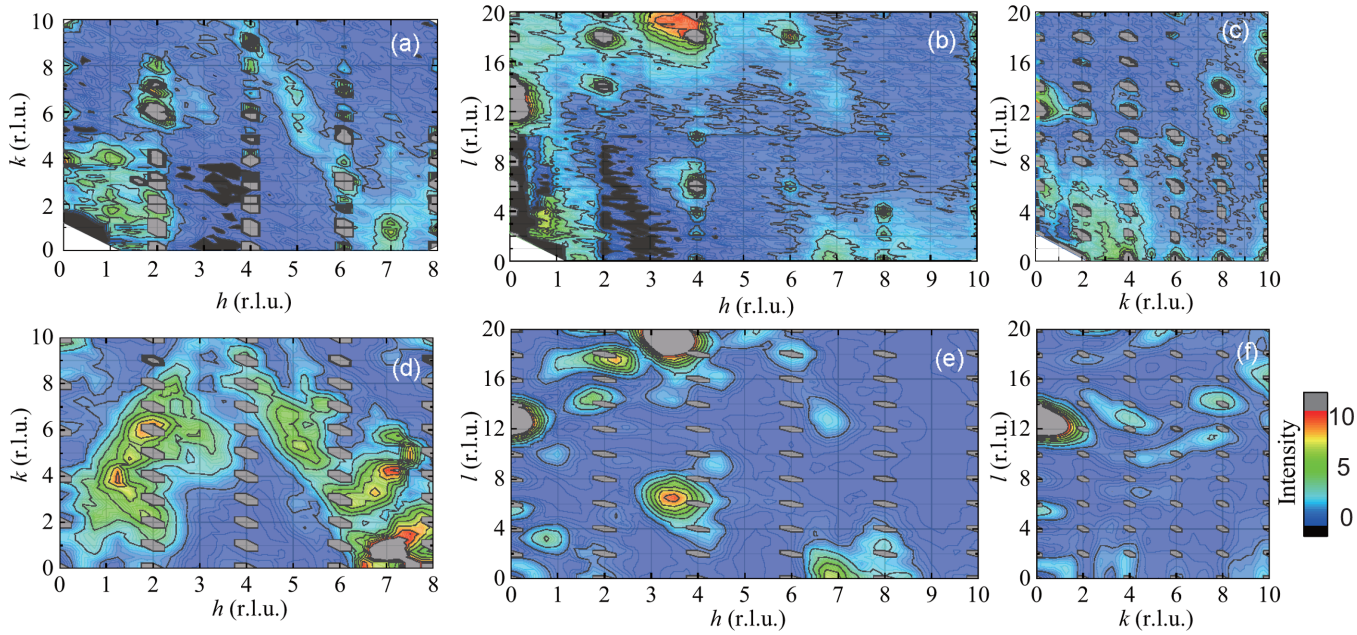

FIG. 2. (a)–(c) TDS intensity distribution on the ($hk0$), ($h0l$), and ($0kl$) planes measured with Mo $K\alpha$ x ray. Bragg peak positions were not measured. Air scattering and linear background were subtracted for presentation. (d)–(f) Those calculated with the Einstein approximation for the 25 lowest energy phonon branches.

for the presentation. A strong diffuse scattering signal was observed in several regions in the reciprocal space.

Long-wavelength acoustic-mode phonons afford strong diffuse signals around strong Bragg reflections. Conventionally, the long-wavelength acoustic-mode phonons are assumed to displace the unit cell without local deformation. Based on this assumption, the intensity, $I_{\rm aco}^{\rm TDS}$, at the scattering vector $\boldsymbol{Q}$ is written as [46]

$$I_{\rm aco}^{\rm TDS}(\boldsymbol{Q}) = \sum_s (\boldsymbol{Q}\cdot\boldsymbol{u}_s)^2 |F^{\rm cell}(\boldsymbol{G})|^2/\omega_{\boldsymbol{q},s}^2, \qquad (1)$$

where s is the branch index, $\boldsymbol{u}_s$ is the polarization vector, $\boldsymbol{G}$ is a reciprocal lattice vector, $F^{\rm cell}(\boldsymbol{G})$ denotes the structure factor for the Bragg peak, and $\omega_{\boldsymbol{q},s}$ denotes the frequency of a phonon characterized by the wave vector $\boldsymbol{q} = \boldsymbol{Q} - \boldsymbol{G}$. Since $\omega_{\boldsymbol{q},s}$ is proportional to $|\boldsymbol{q}|$ for small $\boldsymbol{q}$, the diffuse signal intensity around a Bragg peak originating from the acoustic-mode phonons is proportional to $1/q^2$. The longitudinal acoustic (LA) mode is observed under the condition of $\boldsymbol{Q}$ parallel to both $\boldsymbol{u}_s$ and $\boldsymbol{q}$, and the transverse acoustic (TA) modes are measured under the condition that $\boldsymbol{Q}$ is parallel to $\boldsymbol{u}_s$ and perpendicular to $\boldsymbol{q}$ because of the coefficient of $(\boldsymbol{Q}\cdot\boldsymbol{u}_s)^2$ for the intensity.

Conversely, the intensity originating from optical-mode phonons shows a slight $\boldsymbol{q}$ dependence within the Brillouin zone because of their rather flat dispersion. Instead, each optical branch exhibits a characteristic $\boldsymbol{Q}$ dependence of the TDS intensity distribution through the spatial correlation of the atomic displacement. Therefore, one can examine the atomic displacement caused by the low-energy phonon modes based on the TDS intensity distribution.

This is the principle of the examination of phonons used in Refs. [47,48]. However, one has to be careful to interpret the TDS intensity distribution as it strongly reflects the molecular structure through $F^{\rm cell}$ in Eq. (1). The acoustic-mode phonons in crystals composed of planar molecules always produce an intensity distribution perpendicular to the molecular plane (see Supplemental Material [46] for more details). If we know the eigenmodes constituting a branch, we can calculate the TDS intensity distribution by assuming the phonon energy. Unfortunately, it is practically impossible to calculate the eigenmodes for $\boldsymbol{q}$ in the whole Brillouin zone by the DFT calculations because of the tremendous computational cost. Here, we approximated the atomic displacement of the mth atom in the nth molecule caused by the sth mode, $\boldsymbol{u}_{m,s}(\boldsymbol{R}_n)$, as

$$\boldsymbol{u}_{m,s}(\boldsymbol{R}_n) \propto \frac{\boldsymbol{u}_{m,s}^0}{\omega_s} \exp[i(\boldsymbol{q}\cdot\boldsymbol{R}_n + \phi_{s,q})],$$

where $\boldsymbol{R}_n$ denotes the average position of the nth molecule, $\boldsymbol{u}_{m,s}^0$ denotes the DFT-derived atomic displacement of the mth atom for the mode s at the Γ point, ω_s is the calculated frequency of the mode s, and $\phi_{s,q}$ denotes a random phase factor. We employed the Einstein approximation for the energy; for the a-, b-, and c-polarized acoustic branches, the Γ-point energies of modes 5, 13, and 4 were used for the TDS calculation, respectively. Some examples of the mode-discriminated TDS intensity calculation are presented in Fig. 1.

Figures 2(d)–2(f) show the calculated TDS intensity distribution, derived from the incoherent sum of the scattering intensity from each mode. These calculations reproduce the overall feature of the experimentally observed TDS intensity distribution. Therefore, we employ the above-approximated lattice dynamics as the initial model in our study.

C. Inelastic scattering and phonon dispersion

Figures 3(d)–3(f) show the typical IXS energy spectra measured on the $(6, 1+\eta, 0)$, $(0, 10-\eta, 0)$, and $(0, \eta, 12)$

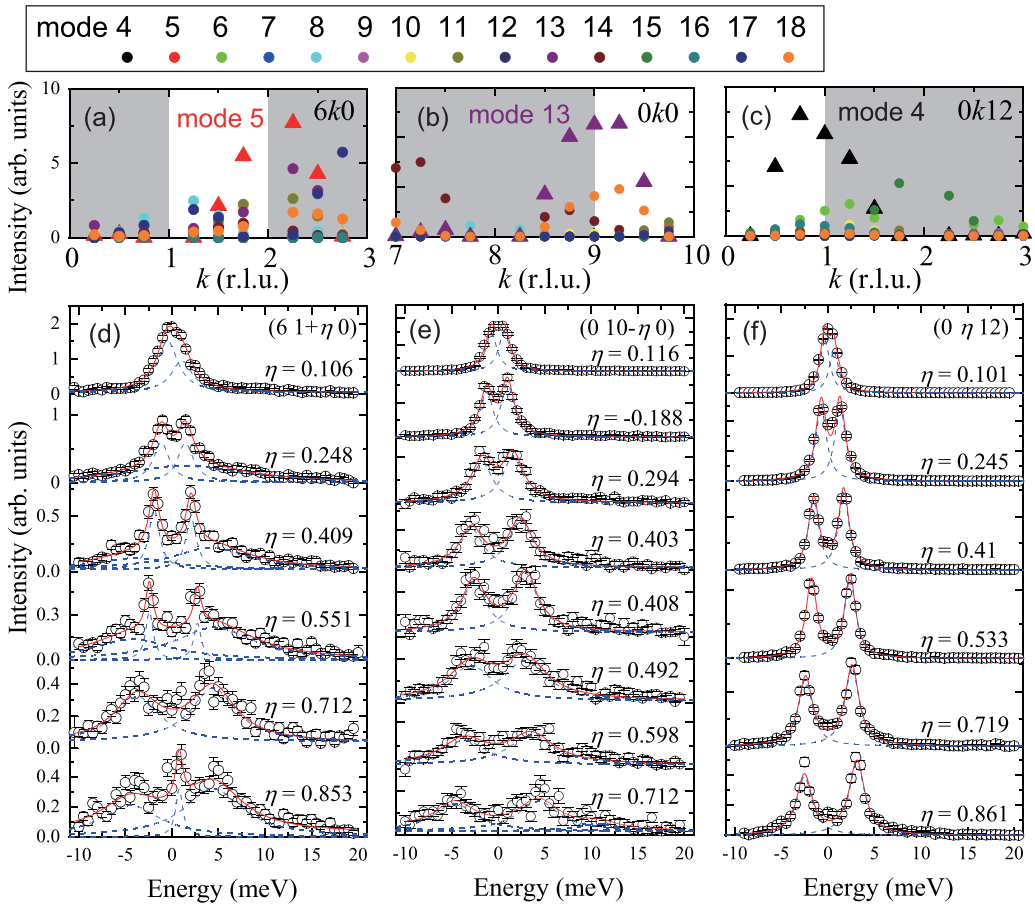

FIG. 3. (a)–(c) Calculated mode-discriminated TDS intensity along the (a) $(6, k, 0)$, (b) $(0, k, 0)$, and (c) $(0, k, 12)$ lines. The calculated intensities of modes 5, 13, and 4, respectively, are indicated with triangles. (d)–(f) Scattered x-ray energy spectra at $(6, 1 + \eta, 0)$, $(0, 10 - \eta, 0)$, and $(0, \eta, 12)$. Strong Bragg reflections are observed at the $\eta = 0$ positions; thus, the $\eta < 0.5$ regions display strong signals from the acoustic modes. The bright regions in panels (a)–(c) show the range of IXS measurements shown in panels (d)–(f). The $\eta > 0.5$ regions are dominated by modes 5, 13 and 4, respectively.

lines, respectively. There are strong Bragg reflections at $\eta = 0$ points; thus, the acoustic-mode phonon signal having atomic displacements along the a, b, and c directions should be strong at small η regions for the three lines, respectively. In the $\eta > 0.5$ region, the phonons in the next Brillouin zone are measured. The peak positions reflect the phonon energy of the optical modes characterized by the wave vector $(0, 1 - \eta, 0)$. Figures 3(a)–3(c) show the calculated mode-discriminated TDS intensity along the measured lines. Based on the calculation, modes 5, 13, and 4 are expected to provide the strongest signal in $\eta > 0.5$ for panels (d)–(f), respectively. Following this procedure, we selected the $\boldsymbol{Q}$ vector for the IXS measurements to obtain the energy of certain modes.

The molecular displacement of mode 5 at the Γ point is presented in Fig. 1(a). Although it involves some amount of atomic displacement parallel to the b axis, this mode is similar to the a-polarized TA mode characterized by the wave vector (0,1,0), which is outside the first Brillouin zone. Therefore, the connection of mode 5 to the a-polarized acoustic mode at the (0,0.5,0) position is reasonable. Additionally, similar relations are found for modes 13 and 4 for the b- and c-polarized acoustic modes, respectively.

The extracted phonon dispersions along the a^*, b^*, and c^* directions are summarized in Fig. 4(b) together with the calculated dispersion. The symbol color shows the measured line in the $\boldsymbol{Q}$ space, the symbol shape shows the vibrational mode, and the open symbols show the calculated ones.

The DFT calculation reproduces the dispersion curves well, particularly along the $\boldsymbol{c}^*$ direction, except for the overestimation of the phonon energy by 10%–20% on average. The largest discrepancy between the calculation and the experiment was found in the LA mode (red circles) and the branch having mode 13 characters (orange squares) on the $(0\eta0)$ line. We presume that the discrepancy is attributed to the finite temperature effect on the crystal structure, or the thermal expansion; use of the larger lattice parameters for the calculation may lead to better agreement with the experiment performed at the room temperature. The effect of the lattice parameters on the vibrational properties has been discussed in Ref. [31].

The measured LA mode on the $(0\eta0)$ line appears missing in the small η region; red closed circles in Fig. 4(b) fall on the a-polarized TA branch. This result will be discussed later.

The shape of the Brillouin zone is presented in Fig. 4(a). The line along the $(\xi00)$ line goes across the X point ($\xi \sim$

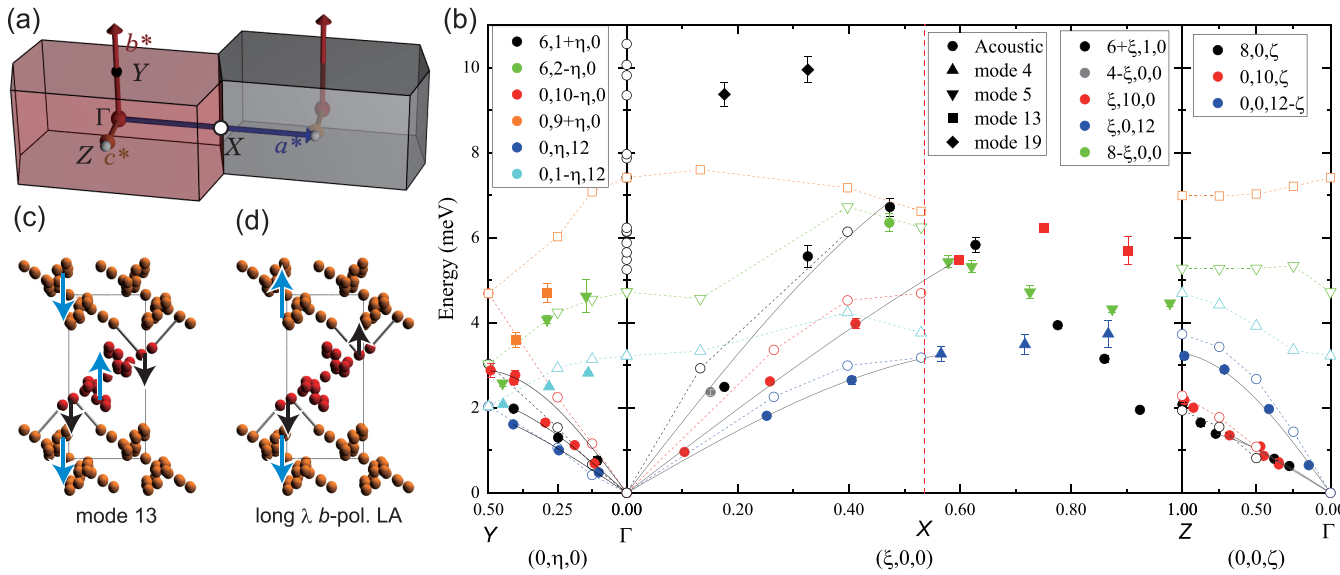

FIG. 4. (a) Brillouin zone and (b) phonon dispersion relation of rubrene. Symbol colors for the experimental results (closed symbols), exhibiting the scattering vectors for the IXS measurements, and the symbol shape represents the mode. The black solid curves show the result of the fitting of the acoustic modes to $A\sin(Bq)$. The vertical dashed line shows the X point. The open symbols show the result of the DFT calculation; open circles on the Γ point show the calculated optical modes 6–12 and 14–20 (some of them are too close to be discriminated on the figure). The dashed lines are guides to the eyes. (c) Schematic view of mode 13 within the a-b plane. The square shows the size of the unit cell. The gray lines connecting the molecules drawn in orange and red indicate the strong intermolecular interaction path [35]. The blue arrows indicate the displacement of the center of gravity, and the black arrows indicate the intramolecular displacement. (d) That of the long-wavelength b-polarized LA mode.

0.53) and subsequently along the zone boundary. The wave vector (100) points to the Z point, the same wave vector with (001). The Γ-X line indicates $\boldsymbol{q} = (\xi, 0, 0)$, while the X-Z line indicates $\boldsymbol{q} = (1-\xi, 0, 1)$.

The dispersion curves on the (ξ00) line show that the a-polarized acoustic mode (black circles on Γ-X) is connected to mode 5 (green upside-down triangles on X-Z), and the b-polarized acoustic mode (red circles on Γ-X) is connected to mode 13 (red squares on X-Z). In addition to the above-mentioned Y point, (0, 0.5, 0), we found the correspondence between these two sets of modes also at the X point.

IV. DISCUSSION

A. Long-wavelength limit

The diagonal elements of the elastic stiffness, c_{ii}, are derived from the slopes of the acoustic-mode phonon dispersion curves at the Γ point. The slopes were extracted by fitting to $A\sin(Bq)$, where A and B are the fitting parameters; the results of the fitting are represented in Fig. 4(b) by the solid black curves. The obtained elastic stiffness is summarized in Table I. The values are similar to those obtained by previous Brillouin scattering experiments [49], showing good agreement in the long-wavelength limit except for a systematic difference of ~25%.

B. Mixing of the local and nonlocal modes

One of the most interesting issues in the phonon dispersion of molecular materials is the $\boldsymbol{q}$ dependence of the local and nonlocal mode mixing. Let us examine the effect of the mixing of the local and nonlocal modes. The spectra along the $(0, 10-\eta, 0)$ line shown in Fig. 3 were measured to observe the LA mode along the $\boldsymbol{b}^*$ direction; notably, the signal has the same energy as that in the TA mode, as shown in Fig. 4(b). This is uncommon because conventionally, the frequency of the LA mode is nearly two times higher than that of the TA modes. Actually, the elastic constant c_{22} estimated by the phonon energy close to the zone boundary, $\eta \sim 0.4$ in Fig. 4(b), agrees well with the calculation and previous reports [49]. Therefore, it is likely that the inelastic signal measured at $(0, 10-\eta, 0)$ reflects the TA mode in the low η region. Considering the a-polarized long-wavelength acoustic phonons, the polarization vector $\boldsymbol{u}_s$ in Eq. (1) is parallel to $\boldsymbol{a}$. In other words, the whole unit cell rigidly displaces along the $\boldsymbol{a}$ direction. In such a situation, we expect no signal for the a-polarized phonon on the (0k0) line, as $\boldsymbol{Q}\cdot\boldsymbol{u}_s = 0$. Experimentally, we observe the TA mode phonon on the

TABLE I. Elastic stiffness of rubrene obtained by IXS (present work), DFT calculations (present work and DFT with optB86b-vdW [49]), and Brillouin scattering [49] (BS) in GPa.

	IXS	DFT	BS [49]	DFT [49]
c_{11}	10.7 ± 1.3	17.7	13.39 ± 0.10	17.0 ± 1.0
c_{22}	11.6 ± 1.5	13.2	14.3 ± 0.4	13.9 ± 1.0
c_{33}	12.4 ± 0.6	21.7	18.48 ± 0.08	25.3 ± 1.1
c_{44}	2.6 ± 0.1	3.6	2.80 ± 0.10	4.4 ± 0.4
c_{55}	2.19 ± 0.04	3.5	6.80 ± 0.04	3.7 ± 0.5
c_{66}	3.9 ± 0.2	7.4	6.46 ± 0.17	6.7 ± 0.4

(0k0) line. This means the eigenmodes of the a-polarized TA mode phonons involve the atomic displacement along the $\boldsymbol{b}$ direction. This should be the character of mode 5, which is connected to the a-polarized acoustic mode. Based on the experimental result, even a $\boldsymbol{q}$ as small as $0.1\boldsymbol{b}^*$, i.e., wavelength of 140 Å, is enough to involve noticeable atomic displacement along the $\boldsymbol{b}$ direction. In other words, the low-energy acoustic-mode phonons in rubrene are associated with significant molecular deformation, attributed to the mixing of the local and nonlocal modes.

Let us examine the atomic displacement in the LA mode. Figure 4(c) shows a schematic view of mode 13 within the a-b plane. The gray lines connecting the molecules drawn in orange and red show the strong intermolecular interaction path [35]. The blue arrows show the displacement of the center of gravity, and the black arrows show the intramolecular displacement. The molecular displacement of the center of gravity is identical to that in the b-polarized LA mode characterized by the wave vector (0,1,0). The intermolecular interaction is highly anisotropic, and the molecular bending in the tetracene backbone is induced by the conflict between the inertia of the central molecule and the surrounding ones. Following this picture, we developed a simple model for the long-wavelength LA mode, as presented in Fig. 4(d). The central molecule has no displacement on average, while both ends are pulled by the surrounding molecules, which results in the librational motion. This is different from the translational motion we originally assumed for the long-wavelength limit. This mode is similar to mode 22, which involves librational motion (see Supplemental Material [46] for the atomic motion). Our mode-discriminated TDS calculation shows that the phonons having mode 22 characters provide low-intensity signals at $(0, 10-\eta, 0)$ even with a rather large amplitude. This explains why high-intensity signals corresponding to the b-polarized LA mode were not observed in Fig. 3(e).

V. SUMMARY

The low-energy phonon modes in the most studied organic semiconductor, rubrene, were clearly observed experimentally, and the modes were characterized by DFT calculations. The procedure to measure the phonon energies of particular modes was demonstrated; using the calculated phonon modes at the Γ point, mode-discriminated TDS was calculated, and the IXS measurements at which strong TDS is expected for a certain mode provides the phonon energy for the mode. Such measurements revealed that the b-polarized LA mode involves librational motion in the small $\boldsymbol{q}$ region, while it involves molecular bending in the large $\boldsymbol{q}$ region. This knowledge of the lattice dynamics provides a robust foundation for the study of electron transport, thermoelectric, and finite-temperature electronic properties of organic semiconductors, as well as a good starting point for understanding the lattice dynamics of highly anisotropic motifs.

ACKNOWLEDGMENTS

The authors thank S. Miyagawa and S. Nakagami for their help in the inelastic x-ray scattering experiment. The authors also thank H. Ishii, N. Kobayashi, and S. Obata for discussion. This work was supported by the MEXT Elements Strategy Initiative to MEXT Elements Strategy Initiative, JPMXP0112101001. The synchrotron radiation experiments were performed with the approval of the Japan Synchrotron Radiation Research Institute (Proposals No. 2018B1108, No. 2019A1147, and No. 2020A1783). Numerical calculations were performed using the supercomputer facilities at National Institute for Materials Research and the Institute for Solid State Physics, the University of Tokyo.

[1] P. Lee, T. Rice, and P. Anderson, Conductivity from charge or spin density waves, Solid State Commun. **14**, 703 (1974).

[2] V. Coropceanu, J. Cornil, D. da Silva Filho, Y. Olivier, R. Silbey, and J.-L. Brédas, Charge transport in organic semiconductors, Chem. Rev. **107**, 926 (2007).

[3] A. Girlando, L. Grisanti, M. Masino, I. Bilotti, A. Brillante, R. G. Della Valle, and E. Venuti, Peierls and Holstein carrier-phonon coupling in crystalline rubrene, Phys. Rev. B **82**, 035208 (2010).

[4] F. Bussolotti, J. Yang, T. Yamaguchi, K. Yonezawa, K. Sato, M. Matsunami, K. Tanaka, Y. Nakayama, H. Ishii, N. Ueno, and S. Kera, Hole-phonon coupling effect on the band dispersion of organic molecular semiconductors, Nat. Commun. **8**, 173 (2017).

[5] M. Matsuura, T. Sasaki, S. Iguchi, E. Gati, J. Müller, O. Stockert, A. Piovano, M. Böhm, J. T. Park, S. Biswas, S. M. Winter, R. Valentí, A. Nakao, and M. Lang, Lattice Dynamics Coupled to Charge and Spin Degrees of Freedom in the Molecular Dimer-Mott Insulator κ-(BEDT-TTF)$_2$Cu[N(CN)$_2$]Cl, Phys. Rev. Lett. **123**, 027601 (2019).

[6] J. Pouget and S. Ravy, X-ray evidence of charge density wave modulations in the magnetic phases of (TMTSF)$_2$PF$_6$ and (TMTTF)$_2$Br, Synth. Met. **85**, 1523 (1997).

[7] N. Kobayashi and M. Ogata, Coexistence of SDW and CDW in quarter-filled organic conductors, J. Phys. Soc. Jpn. **66**, 3356 (1997).

[8] D. Jerome, A. Mazaud, M. Ribault, and K. Bechgaard, Superconductivity in a synthetic organic conductor (TMTSF)$_2$PF$_6$, J. Phys. Lett. **41**, 95 (1980).

[9] I. Samuel and G. Turnbull, Organic semiconductor lasers, Chem. Rev. **107**, 1272 (2007).

[10] R. W. I. de Boer, M. Gershenson, A. Morpurgo, and V. Podzorov, Organic single-crystal field-effect transistors, Phys. Status Solidi A **201**, 1302 (2004).

[11] V. Podzorov, E. Menard, A. Borissov, V. Kiryukhin, J. A. Rogers, and M. E. Gershenson, Intrinsic Charge Transport on the Surface of Organic Semiconductors, Phys. Rev. Lett. **93**, 086602 (2004).

[12] J. Takeya, M. Yamagishi, Y. Tominari, R. Hirahara, Y. Nakazawa, T. Nishikawa, T. Kawase, T. Shimoda, and S. Ogawa, Very high-mobility organic single-crystal transistors

with in-crystal conduction channels, Appl. Phys. Lett. **90**, 102120 (2007).
[13] S. Ciuchi, S. Fratini, and D. Mayou, Transient localization in crystalline organic semiconductors, Phys. Rev. B **83**, 081202(R) (2011).
[14] Z. Shuai, L. Wang, and Q. Li, Evaluation of charge mobility in organic materials: From localized to delocalized descriptions at a first-principles level, Adv. Mater. **23**, 1145 (2011).
[15] H. Ishii, K. Honma, N. Kobayashi, and K. Hirose, Wave-packet approach to transport properties of carrier coupled with intermolecular and intramolecular vibrations of organic semiconductors, Phys. Rev. B **85**, 245206 (2012).
[16] H. Ishii, N. Kobayashi, and K. Hirose, Charge transport calculations by a wave-packet dynamical approach using maximally localized Wannier functions based on density functional theory: Application to high-mobility organic semiconductors, Phys. Rev. B **95**, 035433 (2017).
[17] S. Fratini, M. Nikolka, A. Salleo, G. Schweicher, and H. Sirringhaus, Charge transport in high-mobility conjugated polymers and molecular semiconductors, Nat. Mater. **19**, 491 (2020).
[18] K. Pernstich, B. Rössner, and B. Batlogg, Field-effect-modulated Seebeck coefficient in organic semiconductors, Nat. Mater. **7**, 321 (2008).
[19] H. Kojima, R. Abe, F. Fujiwara, M. Nakagawa, K. Takahashi, D. Kuzuhara, H. Yamada, Y. Yakiyama, H. Sakurai, T. Yamamoto, H. Yakushiji, M. Ikeda, and M. Nakamura, Universality of the giant Seebeck effect in organic small molecules, Mater. Chem. Front. **2**, 1276 (2018).
[20] Y. Kiyota, T. Kawamoto, and T. Mori, Temperature dependence of field-effect thermoelectric power in rubrene crystals, J. Phys. Chem. C **124**, 22399 (2020).
[21] H. Yi, Y. Gartstein, and V. Podzorov, Charge carrier coherence and Hall effect in organic semiconductors, Sci. Rep. **6**, 23650 (2016).
[22] I. Natkaniec, E. Bokhenkov, B. Dorner, J. Kalus, G. MacKenzie, G. Pawley, U. Schmelzer, and E. Sheka, Phonon dispersion in d_8-naphthalene crystal at 6K, J. Phys. C: Solid State Phys. **13**, 4265 (1980).
[23] E. Venuti, R. G. Della Valle, L. Farina, A. Brillante, M. Masino, and A. Girlando, Phonons and structures of tetracene polymorphs at low temperature and high pressure, Phys. Rev. B **70**, 104106 (2004).
[24] Y. Yi, V. Coropceanu, and J.-L. Brédas, Nonlocal electron-phonon coupling in the pentacene crystal: Beyond the Γ-point approximation, J. Chem. Phys. **137**, 164303 (2012).
[25] Z. Tu, Y. Yi, V. Coropceanu, and J.-L. Brédas, Impact of phonon dispersion on nonlocal electron-phonon couplings in organic semiconductors: The naphthalene crystal as a case study, J. Phys. Chem. C **122**, 44 (2018).
[26] T. Otaki, T. Terashige, J. Tsurumi, T. Miyamoto, N. Kida, S. Watanabe, T. Okamoto, J. Takeya, and H. Okamoto, Evaluations of nonlocal electron-phonon couplings in tetracene, rubrene, and C_{10}-DNBDT-NW based on density functional theory, Phys. Rev. B **102**, 245201 (2020).
[27] E. Venuti, I. Bilotti, R. Della Valle, A. Brillante, P. Ranzieri, M. Masino, and A. Girlando, Polarized Raman spectra of a rubrene single crystal, J. Phys. Chem. C **112**, 17416 (2008).
[28] X. Xie, A. Santana-Bonilla, and A. Troisi, Nonlocal electron-phonon coupling in prototypical molecular semiconductors from first principles, J. Chem. Theory Comput. **14**, 3752 (2018).
[29] M. Ruggiero, S. Ciuchi, S. Fratini, and G. D'Avino, Electronic structure, electron-phonon coupling, and charge transport in crystalline rubrene under mechanical strain, J. Phys. Chem. C **123**, 15897 (2019).
[30] G. Schweicher, G. D'Avino, M. Ruggiero, D. Harkin, K. Broch, D. Venkateshvaran, G. Liu, A. Richard, C. Ruzié, J. Armstrong, A. Kennedy, K. Shankland, K. Takimiya, Y. Geerts, J. Zeitler, S. Fratini, and H. Sirringhaus, Chasing the 'killer" phonon mode for the rational design of low-disorder, high-mobility molecular semiconductors, Adv. Mater. **31**, 1902407 (2019).
[31] F. Brown-Altvater, T. Rangel, and J. Neaton, *Ab initio* phonon dispersion in crystalline naphthalene using van der Waals density functionals, Phys. Rev. B **93**, 195206 (2016).
[32] R. Kato, H. Sawa, S. Aonuma, M. Tamura, M. Kinoshita, and H. Kobayashi, Preparation and physical properties of an alloyed $(DMe\text{-}DCNQI)_2Cu$ with fully deuterated DMe-DCNQI ($DMe\text{-}DCNQI = 2,5\text{-}dimethyl\text{-}N,N'\text{-}dicyanoquinonediimine$), Solid State Commun. **85**, 831 (1993).
[33] A. Ueda, S. Yamada, T. Isono, H. Kamo, A. Nakao, R. Kumai, H. Nakao, Y. Murakami, K. Yamamoto, Y. Nishio, and H. Mori, Hydrogen-bond-dynamics-based switching of conductivity and magnetism: A phase transition caused by deuterium and electron transfer in a hydrogen-bonded purely organic conductor crystal, J. Am. Chem. Soc. **136**, 12184 (2014).
[34] Y. Wakabayashi, J. Takeya, and T. Kimura, Sub-Å Resolution Electron Density Analysis of the Surface of Organic Rubrene Crystals, Phys. Rev. Lett. **104**, 066103 (2010).
[35] V. Hathwar, M. Sist, M. Jørgensen, A. Mamakhel, X. Wang, C. Hoffmann, K. Sugimoto, J. Overgaard, and B. Iversen, Quantitative analysis of intermolecular interactions in orthorhombic rubrene, IUCrJ **2**, 563 (2015).
[36] RefCode QQQCIG01, Cambridge Crystallographic Data Centre.
[37] A. Q. R. Baron, Y. Tanaka, S. Goto, K. Takeshita, T. Matsushita, and T. Ishikawa, An X-ray scattering beamline for studying dynamics, J. Phys. Chem. Solids **61**, 461 (2000).
[38] P. E. Blöchl, Projector augmented-wave method, Phys. Rev. B **50**, 17953 (1994).
[39] P. Giannozzi, S. Baroni, N. Bonini, M. Calandra, R. Car, C. Cavazzoni, D. Ceresoli, G. L. Chiarotti, M. Cococcioni, I. Dabo *et al.*, QUANTUM ESPRESSO: a modular and open-source software project for quantum simulations of materials, J. Phys.: Condens. Matter **21**, 395502 (2009).
[40] P. Giannozzi, Jr., O. Andreussi, T. Brumme, O. Bunau, M. B. Nardelli, M. Calandra, R. Car, C. Cavazzoni, D. Ceresoli, M. Cococcioni *et al.*, Advanced capabilities for materials modelling with QUANTUM ESPRESSO, J. Phys.: Condens. Matter **29**, 465901 (2017).
[41] I. Hamada, van der Waals density functional made accurate, Phys. Rev. B **89**, 121103(R) (2014).
[42] A. Dal Corso, Pseudopotentials periodic table: From H to Pu, Comput. Mater. Sci. **95**, 337 (2014).
[43] M. Callsen and I. Hamada, Assessing the accuracy of the van der Waals density functionals for rare-gas and small molecular systems, Phys. Rev. B **91**, 195103 (2015).

[44] S. Baroni, S. de Gironcoli, A. Dal Corso, and P. Giannozzi, Phonons and related crystal properties from density-functional perturbation theory, Rev. Mod. Phys. **73**, 515 (2001).

[45] A. Dal Corso, Elastic constants of beryllium: a first-principles investigation, J. Phys.: Condens. Matter **28**, 075401 (2016).

[46] See Supplemental Material at http://link.aps.org/supplemental/10.1103/PhysRevB.105.205205 for TDS calculation, list of eigenmodes, and dispersion curves obtained by DFT.

[47] A. Eggeman, S. Illig, A. Troisi, H. Sirringhaus, and P. Midgley, Measurement of molecular motion in organic semiconductors by thermal diffuse electron scattering, Nat. Mater. **12**, 1045 (2013).

[48] S. Illig, A. Eggeman, A. Troisi, L. Jiang, C. Warwick, M. Nikolka, G. Schweicher, S. Yeates, Y. Henri Geerts, J. Anthony, and H. Sirringhaus, Reducing dynamic disorder in small-molecule organic semiconductors by suppressing large-amplitude thermal motions, Nat. Commun. **7**, 10736 (2016).

[49] Y. Zhang, D. Manke, S. Sharifzadeh, A. Briseno, A. Ramasubramaniam, and K. Koski, The elastic constants of rubrene determined by Brillouin scattering and density functional theory, Appl. Phys. Lett. **110**, 071903 (2017).